HHS Public Access

Author manuscript

Nat Photonics. Author manuscript; available in PMC 2018 February 22.

Published in final edited form as:

Nat Photonics. 2016 ; 10: 580–584. doi:10.1038/nphoton.2016.141.

In vivo cellular-resolution retinal imaging in infants and children using an ultracompact handheld probe

Francesco LaRocca[1], **Derek Nankivil**[1], **Theodore DuBose**[1], **Cynthia A. Toth**[2,1], **Sina Farsiu**[1,2], and **Joseph A. Izatt**[1,2,*]

[1]Department of Biomedical Engineering and Fitzpatrick Institute of Photonics, Duke University, Durham, North Carolina 27708, USA

[2]Department of Ophthalmology, Duke University Medical Center, Durham, North Carolina 27710, USA

Enabled by adaptive optics, retinal photoreceptor cell imaging is changing our understanding of retinal structure[1,2], function[3,4], and the pathogenesis of numerous ocular diseases[5]. To date, use of this technology has been limited to cooperative adult subjects due to the size, weight and inconvenience of the equipment, thus excluding study of retinal maturation during human development. Here, we report the design and operation of a handheld probe that can perform both scanning laser ophthalmoscopy and optical coherence tomography of the parafoveal photoreceptor structure in infants and children without the need for adaptive optics. The probe, featuring a compact optical design weighing only 94 g, was able to quantify packing densities of parafoveal cone photoreceptors and visualize cross-sectional photoreceptor substructure in children ranging from 14 months to 12 years. The probe will benefit paediatric research by improving the understanding of retinal development, mal-development, and early onset of disease during human growth.

Retinal photoreceptors are specialized neuronal cells responsible for phototransduction, and are thus a crucial part of the human visual system. The imaging of photoreceptors *in vivo* has enabled targeted, single photoreceptor stimulus systems[6] and an improved understanding of the imaging properties of photoreceptors[7,8], the topographical arrangement of different cone photoreceptor types[1], and the pattern of cone loss in retinal diseases such as macular degeneration and retinitis pigmentosa[9]. However, the complexity and large footprint of previous cameras capable of non-invasive imaging of photoreceptors *in vivo* has limited imaging to patients who are able to sit in an upright position and fixate for several minutes,

* jizatt@duke.edu.

Materials & Correspondence

Correspondence and requests for materials should be addressed to J.A.I.

Competing Financial Interests

During part of this work, J.A.I was Chairman and Chief Scientific Advisor at Bioptigen, Inc. and had corporate, equity, and intellectual property interests (including royalties) in this company. F.L., D.N., T.D., and J.A.I. are inventors on a patent application assigned to Duke University related to this work. Other authors declare no competing financial interests.

Author Contributions

F.L. designed and constructed the optical system, collected data, analysed data, and drafted the manuscript. D.N. developed the mechanical design and edited the manuscript. T.D. contributed the theoretical and mathematical basis for the novel compact telescope design. C.A.T., S.F., and J.A.I provided overall guidance to the project, reviewed and edited the manuscript, and obtained funding to support this research.

thus precluding the ability to image young children. With human foveal development reaching adult characteristics before 10 years of age[10], the inability to image young children prevents the measurement of photoreceptors *in vivo* during crucial periods of retinal maturation. In addition, cone and/or rod degenerations (e.g. Leber congenital amaurosis), Stargardt disease and X-linked retinoschisis are present in children and cannot be investigated at the cellular structural level *in vivo* with current devices.

Currently, retinal images are acquired in young children via compact, handheld devices employing either fundus photography[11], scanning laser ophthalmoscopy (SLO)[12], or optical coherence tomography (OCT)[13–15]. While existing handheld systems utilizing these techniques are of important diagnostic value to physicians, their limited lateral resolution prevents the visualization and quantification of cellular structures such as cone photoreceptors. Adaptive optics technology has been shown to enable photoreceptor visualization by correcting for ocular aberrations due to imperfections in the optics of the human eye[16,17], however, the additional hardware and system modifications required to detect and compensate for wavefront aberrations are currently impractical for use in handheld operation.

Recently, we and others have demonstrated tabletop OCT systems[18–20], compact SLO[21] and handheld, combined SLO and OCT systems[22,23] capable of visualizing parafoveal cone photoreceptors in adult volunteers without adaptive optics. This was achieved in part by utilizing an optimal pupil size to maximize lateral resolution[24] and by simulating and optimizing optical system designs with an accurate optical eye model[23,25]. However, while our prior handheld designs were compact relative to tabletop SLO/OCT systems (especially compared to those employing adaptive optics), at 1.45 kg, they were still relatively heavy for handheld devices and difficult to hold stably for extended periods of time. The main features that constrained the minimum size and weight of these systems were: 1) a 4f relay telescope following the scanners, 2) bulky galvanometer-based optical scanners for both SLO and OCT, and 3) the limited availability of small form factor commercial lenses that could adequately compensate for average human ocular aberrations.

In this Letter, we present a new ultra-compact, dual-modality SLO/OCT handheld probe design capable of parafoveal cone photoreceptor visualization with a weight of only 94 g, which is over an order of magnitude lighter than the prior handheld SLO/OCT designs[22,23], and similarly far lighter than commercially available OCT-only handheld systems, which weigh 1.5 kg or heavier[15]. This design utilizes a combination of three significant innovations that enabled the significant reduction in system size. First, a novel telescope design employing converging rather than collimated light on a scanner was used to reduce the length of the system's telescope compared to standard 4f telescope designs. Second, a single high-speed 2D micro-electromechanical systems (MEMS) scanner was used for both SLO and OCT imaging as an alternative to two sets of larger galvanometer-based optical scanners. Finally, custom lens designs were created to minimize device size while correcting for monochromatic and chromatic aberrations in the optical system (including those of the average human eye).

Conventional SLO and OCT retinal systems employ one or a series of standard 4f imaging telescopes to image the scanner plane into the patient's pupil. In this work, we utilize a novel telescope design which employs light converging on the scanner to enable a substantial reduction in telescope length (described further in Supplementary Section I). Using this technique, we developed the optical design of the ultra-compact SLO/OCT handheld probe as shown in Fig. 1a. Light conveyed to the handheld probe by an optical fibre was collimated by an off-axis parabolic mirror and then focused by an achromatic lens prior to a 1 mm diameter 2D MEMS scanner (Mirrorcle Technologies Inc,. Richmond, CA). Following the scanner, a telescope comprising a combination of custom (L2 and L4) and commercial (L3) lenses was used to magnify the beam from the scanner to create a 2.3 mm beam at the pupil of the eye with 7° field of view (FOV). A commercially available plano-concave lens (L3) (012-0050, OptoSigma, Santa Ana, CA) was located adjacent to the intermediate focal plane of the probe to remove most of the field curvature in the system. Prior to this lens, the curvature, thickness, glass type and position of a custom biconvex lens (L2) was optimized in raytracing software (Radiant Zemax LLC, Redmond, WA) to remove residual field curvature and ensure that the principal plane of the L2 and L3 lens pair was a focal length away from the scanner. The last lens of the telescope, an asymmetric triplet (L4), was optimized to provide a telescope magnification of 2.8, minimize induced monochromatic aberrations, and correct for chromatic aberrations (including the longitudinal chromatic aberration of the eye) across the illumination spectrum. A detailed description of the custom lenses (L2 and L4) is given in Supplementary Section II. Figure 1b illustrates retinal plane spot diagrams demonstrating a near-diffraction limited lateral resolution of 8 μm over a 7° FOV in a model eye[25], which was modified as described in [23] to incorporate the effects of ocular dispersion. Figure 1c depicts the mechanical design (further described in Supplementary Section III) that enables easy focus adjustment of ± 3 dioptres of refraction correction at a form factor of only 7 × 6 × 2.5 cm.

High resolution images of a healthy adult human volunteer were acquired *in vivo* (Fig. 2) demonstrating the capabilities of the ultra-compact SLO/OCT handheld probe. The SLO mosaic image reveals clear depictions of blood vessels and capillaries throughout the retina, and nerve fibre bundles are clearly visible near the bottom left region adjacent to the optic disc. At a smaller FOV, the SLO visualized parafoveal cones as close as 3.6° from the fovea without adaptive optics. Six insets from Fig. 2d–e are magnified by a factor of 1.95 to show further detail. As expected and quantified in these insets, an average decrease in cone packing density across all zoomed insets and all graders at each eccentricity (13,800 ± 950 cones mm^{-2} at 3.9° down to 11,100 ± 400 cones mm^{-2} at 6.2°) was observed radially from the foveal center[2,26,27]. Also acquired with this system were high quality OCT images capable of visualizing all retinal layers visible with conventional tabletop OCT systems[28] as shown centred on the fovea in Fig. 2c. All SLO images were distortion corrected to compensate for the non-linear scan response of the 2D MEMS scanner at high scan speeds (Supplementary Section IV) and the relative positioning between SLO and OCT images was determined by cross-correlating vessel-enhanced depth projections from OCT volumes with SLO images (Supplementary Section V). Cone densities were quantified for each zoomed inset via a manual count of cone photoreceptors performed by three human graders, blinded

to the other graders' markings, at each of three different sub-regions at the same retinal eccentricity (see Methods).

Next, we proceeded to image children ranging from 14 months to 12 years of age with and without pathology. All children were imaged in a supine position during examination under general anaesthesia (GA) under approved research protocols (see Methods). Representative images from the healthy eyes of a 25 month old toddler and 14 month old infant are shown in Fig. 3a–d and 3e–h, respectively, while images from pathological eyes are shown in Fig. 4. As with the adult volunteers, the parafoveal cone mosaic could be visualized and quantified in the small FOV SLO images (Fig. 3b, f), which, to our knowledge, is the first demonstration of cone imaging for this age group. Interestingly, the average measured cone density at a 4.1° eccentricity across all zoomed insets and all graders for the 25 month old toddler (Fig. 3b) was 15,050 ± 1,000 cones mm^{-2}, which is similar to values reported in the literature for adults at the same position relative to the fovea[26]. However, for a 10.7° eccentricity for the 14 month old toddler (Fig. 3d), the average measured cone density was 11,700 ± 700 cones mm^{-2}, which is approximately 50% higher than that expected for adults at this eccentricity[26]. The normal expected variation of cone density in adults at both 4.1° and 10.7° away from the fovea is about 10%[26], and therefore is unlikely to account for the higher cone density we observed in the 14 month old subject at a 10.7° eccentricity. Since the normal ranges of cone densities for children as a function of age and retinal position are still unknown, it is unclear whether these differences indicate any retinal abnormality. Nevertheless, it has been documented that there is a centralward migration of cones with age[29], which suggests that infants and children have higher cone densities than adults beyond a certain distance relative to the fovea. From our measurements, this distance appears to be near 4.2° and less than 10.7° from the fovea for 25 and 14 month old children, respectively. However, before cone densities can be used to diagnose retinal diseases in children, it is clear that a more in-depth investigation, potentially through the use of this handheld probe, would be necessary to determine the normative cone densities values for children of all age groups and retinal positions.

In Fig. 4a–d we document healthy macular vessels and retinal layers in a 2 year old toddler with familial exudative vitreoretinopathy (FEVR), a genetic eye disorder that disrupts the growth and development of blood vessels in the retina. In Fig. 4e–j, retinal images are presented of a 2 year old toddler with X-linked retinoschisis, a hereditary retinal degeneration characterized by vision loss and often widespread abnormal splitting of the retina's neurosensory layers. The infant had a previous surgery involving the retinal surface. Resulting microscopic corrugations of a fine membrane wrinkling the retinal surface are perpendicular to the arcuate nerve fibre layer in Fig. 4e and barely visible at the inner surface in cross section in Fig. 4h (arrowhead) where deeper layers show the classic gaps found in retinoschisis. The membranes coalesce into a thicker surface membrane in Fig. 4g which is elevated off the surface in an adjacent cross section (Fig. 4i) and shown in 3D relative to the retinal surface in Fig. 4j. Figure 4k–n shows images acquired from a 12 year old child with a history of blunt trauma resulting in retinal damage at the centre of the macula creating a macular hole (Fig. 4m in cross-section and Fig. 4n in 3D). At the margin of the hole, gaps within the retina (cystoid spaces) and a separation and disruption of the

outer borders of retina from the underlying tissue are visible (Fig. 4m–n). Away from the region of the hole, the nerve fibre layer (Fig. 4k) and deeper retina (Fig. 4l) appear healthier.

In conclusion, we have demonstrated an ultra-compact SLO/OCT handheld probe weighing only 94 g that is capable of imaging the parafoveal cone mosaic in infants and toddlers for the first time. A substantial decrease in system size was possible through use of a novel telescope design employing converging light at the scanner, a single 2D MEMS scanner for both SLO and OCT imaging, and custom optics optimized with an accurate eye model. With further clinical application investigating parafoveal cone photoreceptor packing densities across different ages and retinal positions, we expect the ultra-compact SLO/OCT probe to have a significant impact on our understanding of retinal development, mal-development, and early onset of diseases during human growth. Additionally, by combining the compact optical probe innovations presented here with other point-scanning imaging systems, previously unattainable form factors may be possible for a variety of applications.

Methods

System design

For both SLO and OCT imaging, light from an 840 ± 35 nm superluminescent diode (SLD) (Superlum, Moscow, Russia) was directed through an 80/20 coupler to an input fibre port on the handheld probe (as shown in Fig. 2a). Backscattered light from the eye was collected through the same fibre used for illumination and directed to a spectrometer (SD800, Bioptigen Inc, Durham, NC) when imaging in OCT mode or an avalanche photodiode (C5460, Hamamatsu, Shizuoka-ken, Japan) when imaging in SLO mode. The remaining end of the 80/20 coupler was connected to a beam dump or a reference arm when imaging in SLO or OCT mode, respectively. Switching between SLO and OCT modes was done manually, but could be automated using electromechanical or electro-optical switches to allow sequential SLO and OCT imaging on a frame-by-frame basis.

SLO images were acquired at 14.8 frames per second (fps) with 500 lines per frame and 675 pixels per line by using a 5 MHz digitizer, applying a 3.7 kHz sinusoidal waveform to the fast axis of the MEMS scanner, and utilizing both the forward and backward sweeps of the sinusoidal scan as separate lines in the frame. For OCT imaging, B-scans were acquired at 40 fps with 500 A-scans/B-scan and 2048 pixels/A-scan, by using a 20 kHz A-scan rate (limited by the speed of the spectrometer) and a 40 Hz sawtooth waveform to the fast axis of the MEMS scanner. The OCT axial resolution and 6 dB falloff range were measured to be 7 μm (in air) and 1.1 mm, respectively.

Experimental setup

SLO and OCT retinal images were acquired sequentially spanning either a 3° × 3°, 6.4° × 8.8°, or 8.8° × 6.4° FOV. Different FOVs were obtained by either changing the orientation of the probe by 90° or varying the voltages supplied to the 2D MEMS scanner utilized for both SLO and OCT imaging modes. Background measurements taken prior to imaging were subtracted from both SLO and OCT images to remove static artefacts including lens reflections and scratches or dust on optical elements. Images were registered and averaged

using an image processing program, ImageJ (National Institutes of Health, Bethesda, MD). The signal-to-noise ratio of the OCT system was 101 dB for a 50 μs integration time and 685 μW illumination power at the sample. The irradiance incident on the eye from the handheld probe during either SLO or OCT imaging was under the American National Standards Institute (ANSI) maximum permissible limit[30] at 685 μW. Raw images were acquired, sinusoidally dewarped, and displayed in real time (14.8 fps) to provide the physician direct feedback from images at the time of capture. After an imaging session, all raw data were saved and more accurate higher order dewarping of images was done in post-processing using the steps described in Section IV of the Supplementary Materials. The additional steps performed in post-processing involved the application of a 4th order polynomial transform and a piece-wise linear transform (determined after imaging a calibration target) and were not applied for real time imaging due to longer processing times. All post-processing required 0.7 seconds per frame in MATLAB (Mathworks, Natick, Massachusetts) and the average computation time for image registration was 0.8 seconds per frame in ImageJ on an Intel® Core^{TM} i7-4930K CPU @ 3.40 GHz.

Cone photoreceptor density measurement

Cone packing densities were measured for three 0.5° FOV areas at the same distance from the fovea within 3° FOV SLO images by three human graders. To calculate cone densities, we manually counted cone photoreceptors in ImageJ software and divided by the area sampled. The retinal area sampled was determined by converting the visual angle or retinal FOV (in degrees) to retinal dimensions (in millimetres) by multiplying the FOV by a retinal magnification factor. The retinal magnification factor for a 24 mm axial length eye is 0.291 mm per degree, and we estimated the magnification factor for other axial lengths using a linear scaling based on each subject's estimated or measured axial length[31]. For subjects that did not have axial length measured, axial lengths were determined by the average axial length given the subject's age[32,33] and refractive error[27,34]. Potential limitations on cone density accuracy includes errors in cone counting and in the estimation of the retinal magnification factor.

Human subjects research

The use of our experimental setup for in vivo imaging of awake adults and children during an examination under anaesthesia (EUA) was approved by the Duke University Health System Institutional Review Board and adhered to the tenets of the Declaration of Helsinki. Informed consent was obtained from all subjects or their guardians. For imaging of children already scheduled for a clinically indicated ophthalmologic EUA, the handpiece was place in a single-use sterile plastic bag with an opening for the distal lens tip. The handheld system allowed for efficient imaging during the procedure and reduced operator fatigue due to the much lighter weight of this probe compared to other handheld probes previously reported for use in examination under anesthesia[13,35]. Imaging sessions with this handheld probe comprised approximately 10 minutes per subject, including SLO imaging at 2 different FOVs (6.4° × 8.8° and 3° × 3°) and OCT volumetric imaging with a 6.4° × 6.4° FOV for multiple regions of the retina near the fovea and optic disc. In this study, 1 healthy adult subject and 5 children ranging from 14 months to 12 years of age with and without

pathology were imaged. Data collected from this research were stored and managed in compliance with guidelines from the Health Insurance Portability and Accountability Act.

Supplementary Material

Refer to Web version on PubMed Central for supplementary material.

Acknowledgments

The authors thank L. Vajzovic, S. Freedman, D. Tran-Viet, S. Mangalesh, and A. Dandridge (Duke University Medical Center) for their assistance with enrolling research participants and with acquiring clinical research data. This research was supported in part by grants from the National Institutes of Health (R21-EY02132, R01-EY023039) and the Hartwell Foundation. D.N. was funded in part by the Fitzpatrick Foundation Scholarship.

References

1. Roorda A, Williams DR. The arrangement of the three cone classes in the living human eye. Nature. 1999; 397:520–522. [PubMed: 10028967]
2. Shemonski ND, et al. Computational high-resolution optical imaging of the living human retina. Nat Photon. 2015
3. Rossi EA, Roorda A. The relationship between visual resolution and cone spacing in the human fovea. Nat Neurosci. 2010; 13:156–157. [PubMed: 20023654]
4. Sincich LC, Zhang Y, Tiruveedhula P, Horton JC, Roorda A. Resolving single cone inputs to visual receptive fields. Nat Neurosci. 2009; 12:967–969. [PubMed: 19561602]
5. Zacharria M, Lamory B, Chateau N. Biomedical imaging: New view of the eye. Nat Photon. 2011; 5:24–26.
6. Sheehy CK, et al. High-speed, image-based eye tracking with a scanning laser ophthalmoscope. Biomed Opt Express. 2012; 3:2611–2622. [PubMed: 23082300]
7. Roorda A, Williams DR. Optical fiber properties of individual human cones. J Vis. 2002; 2:4–4.
8. Liu Z, Kocaoglu OP, Turner TL, Miller DT. Modal content of living human cone photoreceptors. Biomed Opt Express. 2015; 6:3378–3404. [PubMed: 26417509]
9. Duncan JL, et al. High-resolution imaging with adaptive optics in patients with inherited retinal degeneration. Invest Ophthalmol Vis Sci. 2007; 48:3283–3291. [PubMed: 17591900]
10. Hendrickson A, Possin D, Vajzovic L, Toth CA. Histologic Development of the Human Fovea From Midgestation to Maturity. Am J Ophthalmol. 2012; 154:767–778. [PubMed: 22935600]
11. Prakalapakorn SG, Wallace DK, Freedman SF. Retinal imaging in premature infants using the Pictor noncontact digital camera. J AAPOS. 2014; 18:321–326. [PubMed: 25173892]
12. Kelly JP, Weiss AH, Zhou Q, Schmode S, Dreher AW. Imaging a child's fundus without dilation using a handheld confocal scanning laser ophthalmoscope. Arch Ophthalmol. 2003; 121:391–396. [PubMed: 12617711]
13. Scott AW, Farsiu S, Enyedi LB, Wallace DK, Toth CA. Imaging the Infant Retina with a Hand-held Spectral-Domain Optical Coherence Tomography Device. Am J Ophthalmol. 2009; 147:364–373.e362. [PubMed: 18848317]
14. Woonggyu J, et al. Handheld Optical Coherence Tomography Scanner for Primary Care Diagnostics. IEEE Trans Biomed Eng. 2011; 58:741–744. [PubMed: 21134801]
15. Lu CD, et al. Handheld ultrahigh speed swept source optical coherence tomography instrument using a MEMS scanning mirror. Biomed Opt Express. 2014; 5:293–311.
16. Roorda A, et al. Adaptive optics scanning laser ophthalmoscopy. Opt Express. 2002; 10:405–412. [PubMed: 19436374]
17. Dubra A, et al. Noninvasive imaging of the human rod photoreceptor mosaic using a confocal adaptive optics scanning ophthalmoscope. Biomed Opt Express. 2011; 2:1864–1876. [PubMed: 21750765]

18. Potsaid B, et al. Ultrahigh speed Spectral / Fourier domain OCT ophthalmic imaging at 70,000 to 312,500 axial scans per second. Opt Express. 2008; 16:15149–15169. [PubMed: 18795054]
19. Schmoll T, Kolbitsch C, Leitgeb RA. Ultra-high-speed volumetric tomography of human retinal blood flow. Opt Express. 2009; 17:4166–4176. [PubMed: 19259253]
20. Potsaid B, et al. Ultrahigh speed 1050nm swept source / Fourier domain OCT retinal and anterior segment imaging at 100,000 to 400,000 axial scans per second. Opt Express. 2010; 18:20029–20048. [PubMed: 20940894]
21. LaRocca F, Dhalla AH, Kelly MP, Farsiu S, Izatt JA. Optimization of confocal scanning laser ophthalmoscope design. J Biomed Opt. 2013; 18:076015. [PubMed: 23864013]
22. LaRocca F, Nankivil D, Farsiu S, Izatt JA. Handheld simultaneous scanning laser ophthalmoscopy and optical coherence tomography system. Biomed Opt Express. 2013; 4:2307–2321. [PubMed: 24298396]
23. LaRocca F, Nankivil D, Farsiu S, Izatt JA. True color scanning laser ophthalmoscopy and optical coherence tomography handheld probe. Biomed Opt Express. 2014; 5:3204–3216. [PubMed: 25401032]
24. Donnelly WJ III, Roorda A. Optimal pupil size in the human eye for axial resolution. J Opt Soc Am A. 2003; 20:2010–2015.
25. Goncharov AV, Dainty C. Wide-field schematic eye models with gradient-index lens. J Opt Soc Am. 2007; 24:2157–2174.
26. Curcio CA, Sloan KR, Kalina RE, Hendrickson AE. Human photoreceptor topography. J Comp Neurol. 1990; 292:497–523. [PubMed: 2324310]
27. Chui TYP, Song H, Burns SA. Individual Variations in Human Cone Photoreceptor Packing Density: Variations with Refractive Error. Invest Ophthalmol Vis Sci. 2008; 49:4679–4687. [PubMed: 18552378]
28. Staurenghi G, Sadda S, Chakravarthy U, Spaide RF. Proposed Lexicon for Anatomic Landmarks in Normal Posterior Segment Spectral-Domain Optical Coherence Tomography: The IN•OCT Consensus. Ophthalmology. 2014; 121:1572–1578. [PubMed: 24755005]
29. Yuodelis C, Hendrickson A. A qualitative and quantitative analysis of the human fovea during development. Vision Res. 1986; 26:847–855. [PubMed: 3750868]
30. American National Standard Institute (ANSI). American National Standard for the Safe Use of Lasers. American National Standard Institute, Inc; 2000.
31. Cooper RF, Langlo CS, Dubra A, Carroll J. Automatic detection of modal spacing (Yellott's ring) in adaptive optics scanning light ophthalmoscope images. Ophthalmic Physiol Opt. 2013; 33:540–549. [PubMed: 23668233]
32. Gordon RA, Donzis PB. Refractive development of the human eye. Arch Ophthalmol. 1985; 103:785–789. [PubMed: 4004614]
33. Augusteyn RC, et al. Human ocular biometry. Exp Eye Res. 2012; 102:70–75. [PubMed: 22819768]
34. Atchison DA, et al. Eye Shape in Emmetropia and Myopia. Invest Ophthalmol Vis Sci. 2004; 45:3380–3386. [PubMed: 15452039]
35. Chavala SH, et al. Insights into Advanced Retinopathy of Prematurity Using Handheld Spectral Domain Optical Coherence Tomography Imaging. Ophthalmology. 116:2448–2456.

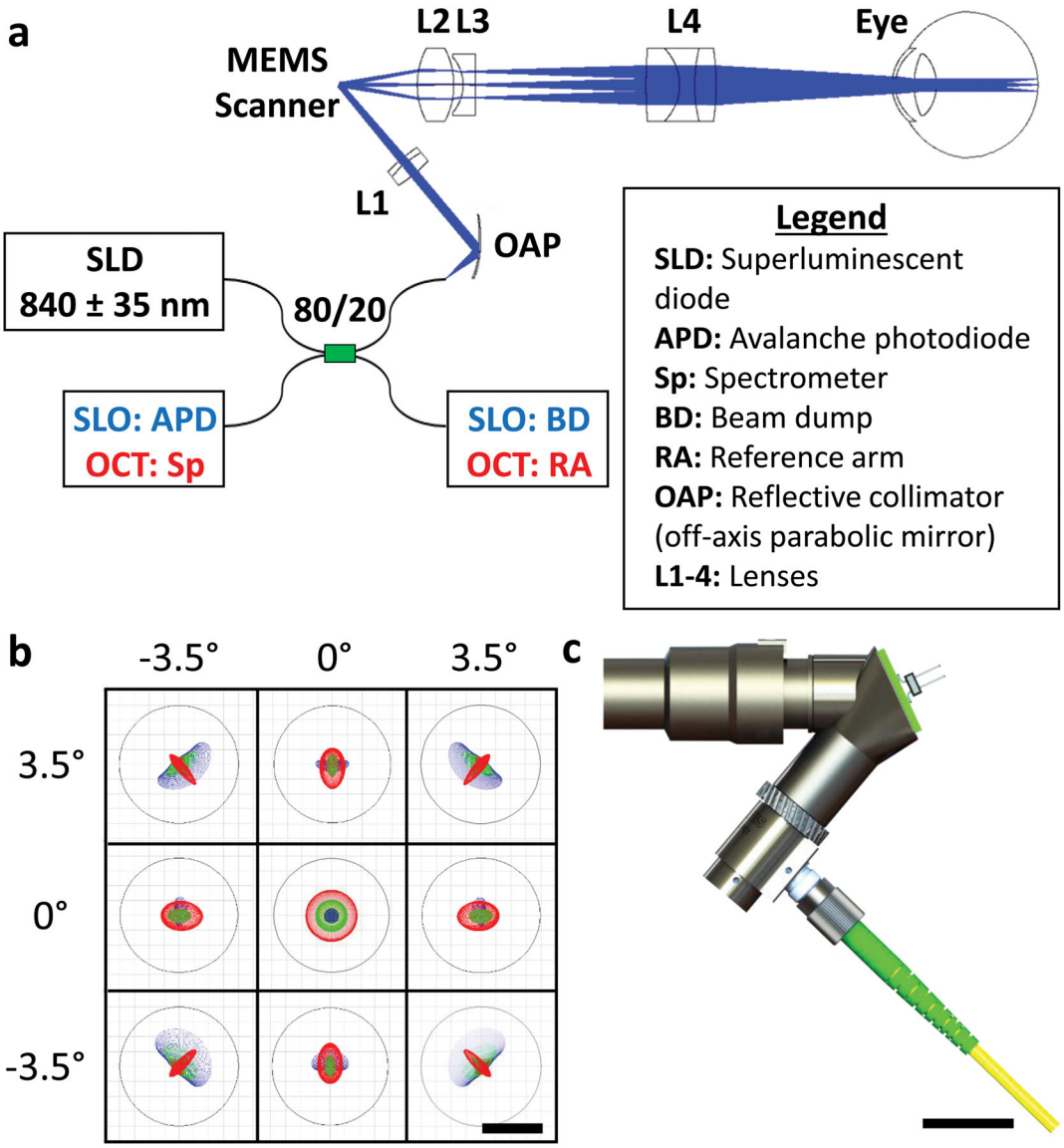

Figure 1.

Optomechanical design of the ultra-compact SLO/OCT handheld probe. a, Optical design and system schematic of the handheld probe. All optical components are labelled and described in the legend. Blue and red text in the schematic correspond to components used for imaging in SLO or OCT mode, respectively. b, Spot diagrams (colour coded for 3 wavelengths spanning 805–870 nm) for both SLO and OCT illumination on the retina of a model eye spanning a 7° FOV. Airy disks are shown by black circles. c, Photorealistic rendering of the handheld probe mechanical design. Scale bars represent 8 μm in b and 2 cm in c.

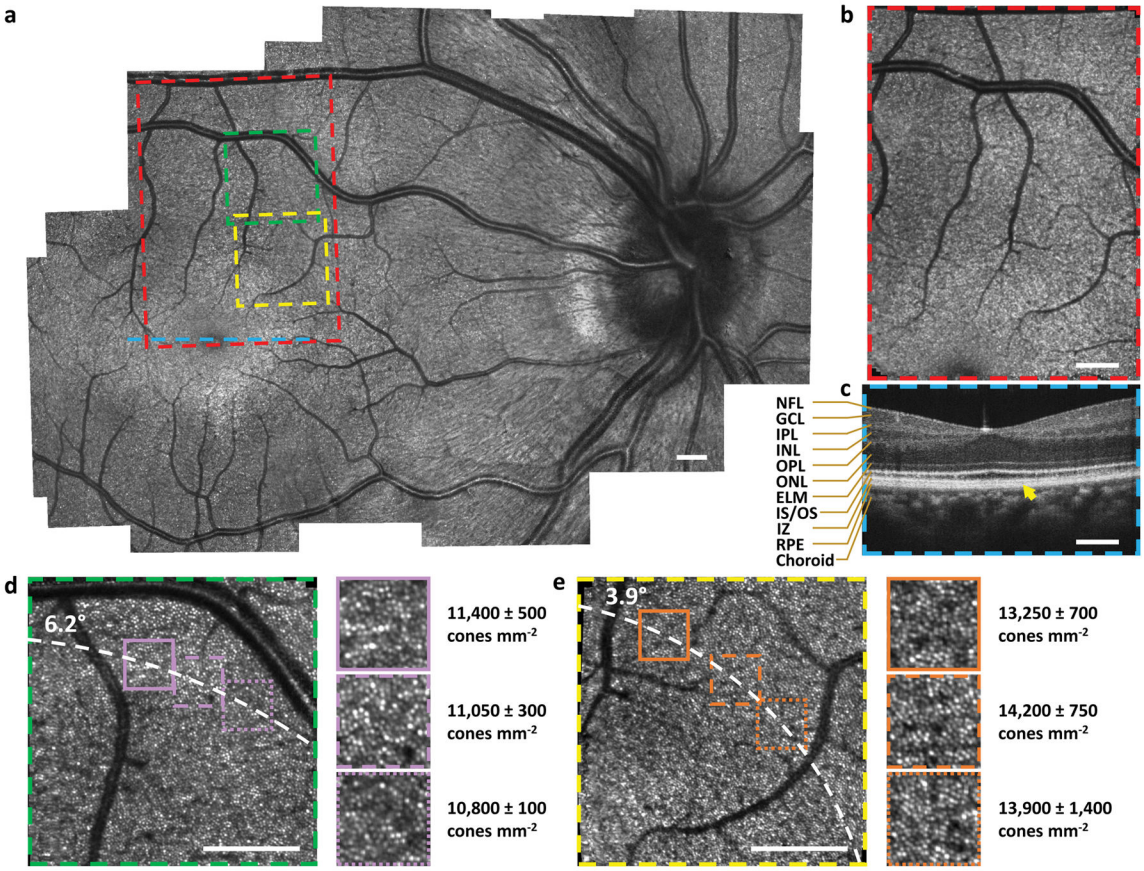

Figure 2.

High resolution retinal images acquired on a healthy adult. a, SLO image mosaic generated from 25 SLO images. b, Single SLO image. c, OCT B-scan at the fovea. NFL: nerve fibre layer, GCL: ganglion cell layer, IPL: inner plexiform layer, INL: inner nuclear layer, OPL: outer plexiform layer, ONL: outer nuclear layer, ELM: external limiting membrane, IS/OS: inner segment/outer segment, IZ: interdigitation zone, RPE: retinal pigment epithelium. d, e, Reduced FOV SLO images visualizing parafoveal photoreceptors. Zoomed insets (1.95×) and cone densities (mean ± one standard deviation as determined by three human graders) are shown to the right of d–e. Coloured boxes and line on the mosaic indicate locations of SLO and OCT images in b–e. Dashed white curves in d–e pass through the centre of zoomed insets at distances of 6.2° and 3.9° from the fovea, respectively. Yellow arrow in c indicates a well-defined interdigitation zone. Scale bars, 1°.

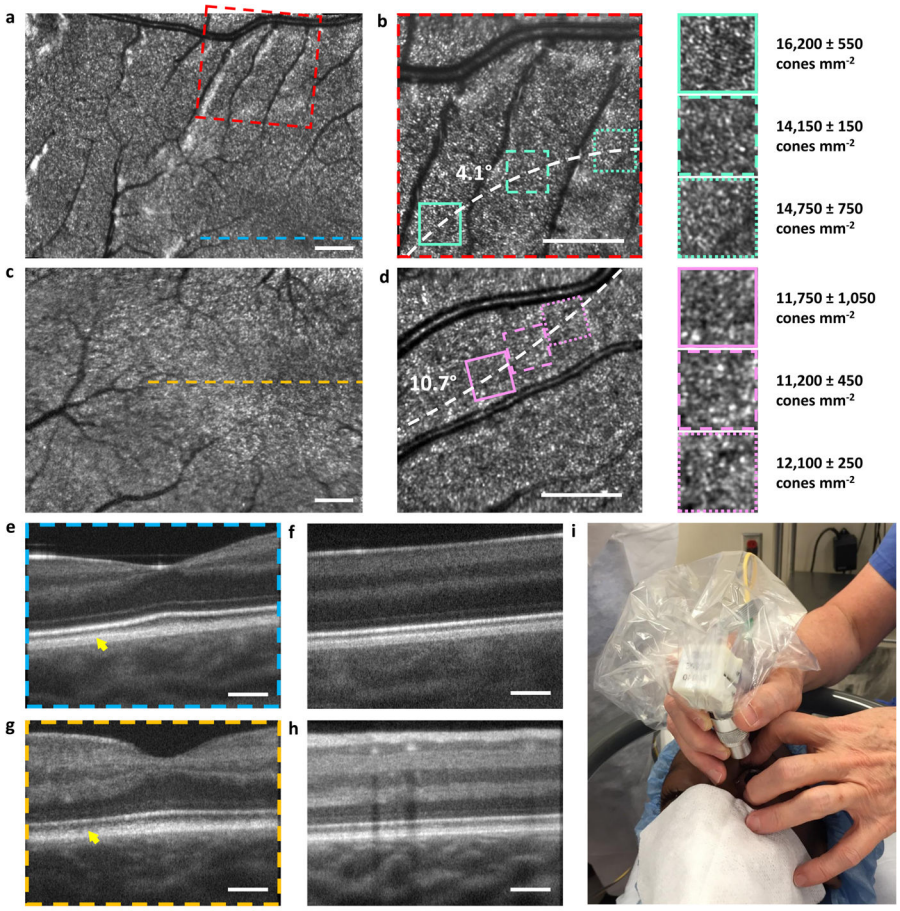

Figure 3.

High resolution retinal images acquired on a healthy 25 month old toddler (a–b, e–f) and 14 month old infant (c–d, g–h). a, c, SLO images acquired near the fovea. b, d, Reduced FOV SLO images visualizing parafoveal photoreceptors. Zoomed insets (1.95×) and cone densities (mean ± one standard deviation as determined by three human graders) are shown to the right of b and d. e–h, OCT B-scans demonstrating similar image quality to that of the adult subject. i, photograph of the handheld probe in use on a child in the operating room. Dashed white curves in b and e pass through the centre of the zoomed insets at distances of 4.1° and 10.7° from the fovea, respectively. The yellow arrows in e and g indicate the interdigitation zone, which is well-defined in the 25 month old toddler but not fully developed in the 14 month old infant. Scale bars, 1°.

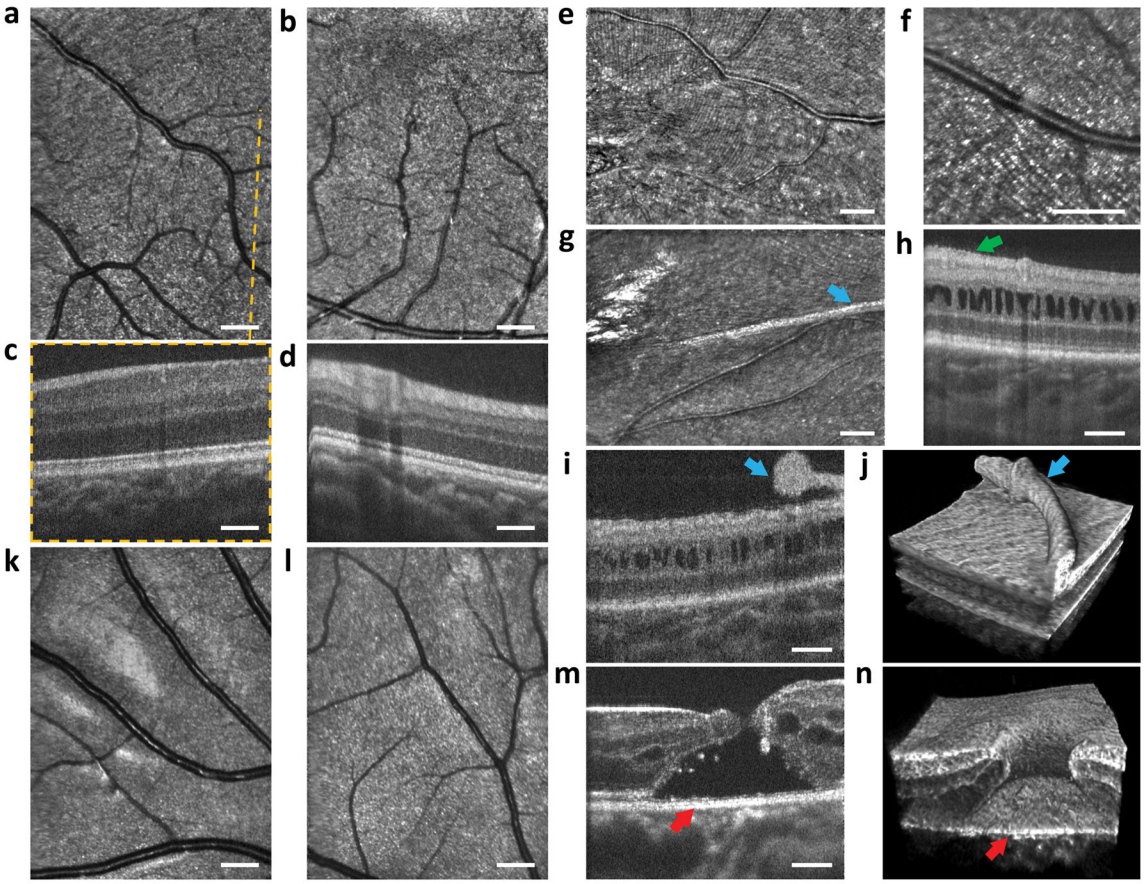

Figure 4.

Imaging results from children with eye disease: a 2 year old toddler with FEVR (a–d), a 2 year toddler with X-linked retinoschisis (e–j) and a 12 year old child with a macular hole (k–n). a–b, SLO images indicating undamaged regions of the macula. c–d, OCT B-scans with no visible abnormality as expected for this disease away from the peripheral retina. e–g, SLO images revealing fine membrane wrinkling of the retinal surface and an elevated, thicker surface membrane. h–j, OCT B-scans and volume showing retinal gaps characteristic of retinoschisis. Green arrow in h shows subtle wrinkling of the epiretinal membrane. Blue arrows in i–j reveal the elevated retinal membrane also visible in the SLO image in g. k–l, SLO images showing minimal damage to areas peripheral to the macular hole. m–n, OCT B-scan and volume showing the macular hole in microscopic detail with red arrows indicating corresponding sections of the hole.